

Self-assembling human heart organoids for the modeling of cardiac development and congenital heart disease

Yonatan Lewis-Israeli

Michigan State University

Aaron Wasserman

Michigan State University

Mitchell Gabalski

Michigan State University

Kristen Ball

Michigan State University

Brett Volmert

Michigan State University

Weiyang Yang

Michigan State University

Bo Li

Michigan State University

Jinyun Zou

Washington University in St. Louis

Guangming Ni

Washington University in St. Louis

Natalia Pajares

Michigan State University

Xanthippi Chatzistavrou

Michigan State University

Chao Zhou

Washington University in St. Louis <https://orcid.org/0000-0002-8679-3413>

Zhen Qiu

Michigan State University

Wen Li

Michigan State University

Aitor Aguirre (✉ aaguirre@msu.edu)

Michigan State University <https://orcid.org/0000-0002-1383-2792>

Article

Keywords: congenital heart defects (CHD), self-assembling human heart organoids, birth defects

Posted Date: December 31st, 2020

DOI: <https://doi.org/10.21203/rs.3.rs-132349/v1>

License:   This work is licensed under a Creative Commons Attribution 4.0 International License.

[Read Full License](#)

Version of Record: A version of this preprint was published at Nature Communications on August 26th, 2021. See the published version at <https://doi.org/10.1038/s41467-021-25329-5>.

Abstract

Congenital heart defects (CHD) constitute the most common birth defect in humans, affecting approximately 1% of all live births. Our ability to understand how these disorders originate is hindered by our limited ability to model the complexity of the human heart *in vitro*. There is a pressing need to develop more faithful organ-like platforms recapitulating complex *in vivo* phenotypes to study human development and disease *in vitro*. Here we report a novel method to generate human heart organoids by self-assembly using pluripotent stem cells. Our method is fully defined, highly efficient, scalable, shows high reproducibility and is compatible with screening and high-throughput approaches. Human heart organoids (hHOs) are generated using a two-step canonical Wnt signaling modulation strategy using a combination of chemical inhibitors and growth factors in completely defined culture conditions. hHOs faithfully recapitulate human cardiac development and are similar to age-matched fetal cardiac tissues at the transcriptomic, structural and cellular level. hHOs develop sophisticated internal chambers with well-organized multi-lineage cell-type regional identities reminiscent of the heart fields and the atrial and ventricular chambers, as well as the epicardium, endocardium, and coronary vasculature, and exhibit functional activity. We also show that hHOs can recreate complex metabolic disorders associated with CHD by establishing the first *in vitro* human model of diabetes during pregnancy (DDP) to study embryonic CHD. morphological and metabolically effects of increased glucose and insulin, showing the capability of modeling the effects of diabetes during pregnancy (DDP). Our heart organoid model constitutes a powerful novel tool for translational studies in human cardiac development and disease.

Introduction

Cardiovascular diseases (CVD) and congenital heart diseases (CHD) are the leading cause of death in the developed world and the most common type of congenital defect in humans, respectively. Despite the importance of understanding human cardiovascular disorders for treatment and prevention, progress on the creation of human heart organoid models for cardiovascular disease studies has been very limited and lags significantly behind the progress that has been achieved for other organs (e.g., kidney, colon, intestine, brain)¹⁻⁴. Human pluripotent stem cells (hPSCs) enable us to recapitulate important developmental steps *in vitro* to produce specific cardiac cell types with relative ease, high purity, and in large amounts^{5,6}. However, current cell models are still far away from the structural and cellular complexity of the tissues and organs they intend to represent (e.g. lack of 3D matrix, disorganized cells, and absence of multicell-type interactions), frequently studying isolated cell types and minimizing or ignoring other heart cells (e.g., epicardial cells, endocardial cells) or the contribution of cell-cell communication to a disease phenotype. There is a strong demand to bridge this technological and knowledge gap, since producing more faithful *in vitro* models of the human heart will allow us to better model health and disease states for research and translational applications.

Significant attempts have been made over the last two decades to produce more complex, multicell-type 3D heart tissue using tissue engineering approaches to cover the need for *in vitro* human heart models. While these approaches allow for high control of the end construct, they tend to be expensive, work-

intensive, and not readily scalable. Furthermore, they do not faithfully represent the original cell composition (e.g., use of dermal fibroblasts or HUVECs) and organization (e.g., cardiospheres) of the heart. These approaches yield functional tissues but fall short in terms of physiological and structural relevance, as well as cell and ECM complexity.

Here, we report a novel small molecule-based methodology to create highly complex and physiological relevant human heart organoids (hHO) using hPSCs by manipulating cardiac developmental programs. Our protocol relies mainly on three sequential Wnt modulation steps (activation/inhibition/activation) at specific time points on suspension embryoid bodies and produces significant heart-like structures in terms of structure, organization, functionality, cardiac cell type complexity, ECM composition, and vascularization. Additionally, our method is cheap compared to growth factor-based approaches and relatively simple in terms of procedure. It is also automatable, scalable, and amenable to high-content/high-throughput pharmacological screenings. As proof-of-concept of the value of this system to model human cardiac disease, we utilized our organoid system to model the effects of diabetes during pregnancy (DDP) on the developing embryonic heart and explore its potential to identify therapeutic targets.

Results

Self-assembling human heart organoids generated by Wnt signaling modulation. Our method was designed to meet four initial milestones: 1) high organoid quality and reproducibility; 2) high-throughput/high-content format; 3) relative simplicity (no need for special equipment outside of traditional cell culture instrumentation); 4) defined chemical conditions for maximum control and versatility for downstream applications. We started by assembling hPSCs into embryoid bodies by centrifugation in ultra-low attachment 96-well plates followed by a 48-hour incubation at 37 °C and 5% CO₂ prior to induction. This incubation allowed for spheroid stabilization and was important to increase efficiency, as other incubation times (12 hours, 24 hours) provided inferior results once differentiation started. After induction, two-thirds of spent medium was removed and replaced with fresh medium for each medium change, resulting in gradual transitions in exposure to the different signals employed. Induction of mesoderm and cardiogenic mesoderm was achieved by sequential exposure to CHIR99021, a canonical Wnt pathway activator (via specific GSK3 inhibition), and Wnt-C59, a Wnt pathway inhibitor (via PORCN inhibition) (Fig. 1a). Brightfield and immunofluorescence imaging of hHOs showed a significant increase in size throughout the differentiation protocol (Fig. 1b). Confocal microscopy of hHOs stained with cardiomyocyte specific TNNT2 antibody showed that organoids started to develop sarcomeres as early as day 7 (Fig. 1b), with clear sarcomere formation and fiber assembly readily apparent by day 15 (Fig. 1c). Beating hHOs appeared as early as day 6 of the differentiation protocol, with robust and regular beating appearing by day 10 in all samples (**Suppl. Videos 1 & 2**). To determine optimal conditions for initial Wnt activation, we exposed embryoid bodies to different concentrations of CHIR99021 (4 μM, 6.6 μM and 8 μM) on day 0 for 24 hours. On day 15, hHOs were evaluated for cardiac lineage formation by confocal microscopy (**Suppl. Figure 1a**). Optimal cardiogenic mesoderm induction

for all hESC and hiPSC lines tested occurred at lower CHIR99021 concentrations than previously reported for cardiomyocyte monolayer differentiation protocols, which typically range from 10 to 12 μM CHIR⁷⁻¹³. A 4 μM CHIR99021 exposure resulted in the highest cardiomyocyte content with $64 \pm 5\%$ TNNT2⁺ cells at day 15, versus $9.6 \pm 5\%$ and $2.4 \pm 2\%$ for 6.6 μM and 8 μM CHIR99021, respectively (Fig. 1d, **Suppl. Figure 1a**). This difference is probably due to endogenous morphogen production and paracrine signaling within the developing hHOs, bestowed by the 3D environment and inherent self-assembling properties of the organoids. hHOs treated with 4 μM CHIR99021 also displayed the best functional properties of the three concentrations (**Suppl. Figure 1b, c**). Our initial hHO differentiation protocol was reproducible across multiple hPSC lines (iPSC-L1, AICS-37-TNNI1-mEGFP, iPSCORE_16_3, H9). hHOs derived from different hPSC lines exhibited similar differentiation efficiencies, beat metrics, and sizes (Fig. 1e, f).

Controlled induction of epicardial lineage in human heart organoids. To increase organoid complexity and produce more developmentally relevant structures, we adapted methods that have been used successfully in monolayer hPSC differentiation for specific induction of epicardial cells¹¹. The method consists of a second activation of canonical Wnt signaling on differentiation days 7–9 to induce secondary cardiac lineages. To determine if this second activation would prime our hHOs to increase complexity and better recapitulate heart development, we tested the effects of a second CHIR99021 exposure on day 7 (Fig. 2a). CHIR99021 was added to developing hHOs at varying concentrations (2, 4, 6 and 8 μM), and exposure lengths (1, 2, 12, 24, and 48 hours). Efficiency of epicardial cell and cardiomyocyte formation was evaluated using confocal imaging and quantification for well-established epicardial (WT1, ALDH1A2, TJP1) and cardiomyocyte (TNNT2) markers at day 15 (Fig. 2b, c; **Suppl. Figure 2a, b**). We found that the treatment robustly promoted the formation of proepicardium and epicardial cells (Fig. 2b-d; **Suppl. Figure 2a**). We found that high concentrations or long exposure times led to marked inhibition in the formation of other cardiac cell types other than epicardial cells, particularly affecting cardiomyocytes formation. We found that a single 2 μM CHIR99021 treatment for 1 hour on differentiation day 7 produced the most physiologically relevant epicardial to myocardial ratio (60% cardiomyocytes, 10–20% epicardial cells) (Fig. 2b, c; **Suppl. Figure 2b, c**). Structurally, a significant part of the epicardial tissue was found on external layers of the organoid and adjacent to well-defined myocardial tissue (TNNT2⁺) (Fig. 2d), thus recapitulating the structural organization found in the heart. The robust expression of TJP1 on epicardial cell membranes also confirmed the epithelial phenotype of these cells (Fig. 2c, d).

Transcriptomic analysis reveals hHOs closely model human fetal cardiac development and produce all main cardiac cell lineages. We decided to perform transcriptomic analysis at different stages of organoid formation to better characterize developmental steps and the molecular identity of cells in the organoids. hHOs were collected at different timepoints (day 0 through day 19) of differentiation (Fig. 3). Unsupervised K-means clustering analysis revealed organoids progressed through three main developmental stages: day 0 – day 1, associated with pluripotency and early mesoderm commitment; day 3 – day 7, associated with early cardiac development; and day 9 – day 19, associated with fetal heart maturation (Fig. 3a, **Suppl. Figure 3**). Gene ontology biological process analysis identified important

genetic circuitry driving cardiovascular development and heart formation (Fig. 3a & **Supp. Table 1**; **raw data deposited in GEO under GSE153185**). To compare cardiac development in hHOs to that of previously existing methods, we performed RNA-seq on monolayer iPSC-derived cardiac differentiating cells using well-established protocols³. We also compared our RNA-seq results to publicly available datasets from previously reported monolayer cardiac differentiation protocols and human fetal heart tissue (gestational age days 57–67)¹⁴ (**GSE106690**). In all instances, hHO cardiac development transcription factor expression regulating first and second heart field specification (FHF, SHF, respectively) was similar to that observed in monolayer PSC-derived cardiac differentiation and corresponded well to that observed in fetal heart tissue (Fig. 3b, **Suppl. Figure 3a**). Interestingly, gene expression profiles showed that hHOs had higher cardiac cell lineage complexity than cells that underwent monolayer differentiation, especially in the epicardial, endothelial, endocardial, and cardiac fibroblast populations (Fig. 3c, **Suppl. Figure 3b-c**). These data suggest a significant enrichment in the structural and cellular complexity of our hHOs, thus bringing them in line with fetal hearts. This was confirmed by extending our gene expression analysis to look at several widespread critical gene clusters involved in classic cardiac function, including conductance, contractile function, calcium handling, and cardiac metabolism, among others (Fig. 3d). Of special interest, hHOs produced significant amounts of heart-specific extracellular matrix, a feature present in the fetal hearts but completely absent in monolayer differentiation protocols (Fig. 3d, **Suppl. Figure 3d**). Principle component analysis showed a clear progression in development in the hHOs from day 0 to 19 (**Suppl. Figure 3e**). Overall, hHOs had individual expression profiles best matching those of fetal hearts, and the global hHO transcriptome was closer to that observed in fetal hearts than in any of the monolayer protocols, as determined by hierarchical clustering (Fig. 3e).

Human heart organoids recapitulate heart field specification and atrial and ventricular chamber formation. The first and second heart fields are two cell populations found in the developing heart. Cells from the FHF contribute to the linear heart tube formation, followed by migrating cells belonging to the SHF that contribute to further expansion and chamber formation¹⁵. We found evidence of cells representing both heart fields in our organoids. *HAND1* (FHF) and *HAND2* (SHF) are members of the Twist family of basic helix-loop-helix (bHLH) transcription factors that play key roles in the regulation of numerous cell types in the developing heart¹⁶. Immunofluorescence of Day 8 hHOs showed well-differentiated, segregated regions of *HAND1* (Fig. 4a) and *HAND2* (Fig. 4d) cells, suggesting that both FHF and SHF progenitors are present and separate into their respective heart fields. In human hearts, the left ventricle ultimately forms from FHF progenitors and the atria form from SHF progenitors¹⁷. We therefore sought to determine whether our hHOs contain cardiomyocytes committed to either the atrial or ventricular lineages. Immunofluorescence for *MYL2* (which encodes myosin light chain-2, ventricular subtype) and *MYL7* (encodes myosin light-chain 2, atrial subtype) in Day 15 hHOs showed cardiomyocytes positive for both subtypes. The two different populations localized to different regions of the organoid and were in close proximity, which mirrors the expression pattern seen in human hearts (Fig. 4c). The expression of *HAND1*, *HAND2*, and *MYL7* transcripts in the hHOs increased throughout the differentiation protocol and were similar to that observed in human fetal hearts, while *MYL2* increased to a lesser degree (**Suppl. Figure 3a, c**). Adding India ink to the media for contrast, we recorded the beating

organoids under a light microscope and observed central chamber-like structures surrounded by beating tissue (**Suppl. Video 3**). Taken together, these data suggest that the differentiation of our hHOs involves heart field formation, chamber specification and cardiomyocyte specification into atrial and ventricular subpopulations, both of which further emphasize their recapitulation of human cardiac development.

Heart organoids produce multiple cell cardiac lineages and acquire cardiac-specific morphological functionality. Results from the transcriptomic analysis (Fig. 3) suggested that the second CHIR99021 exposure led to the formation of other mesenchymal lineages and higher complexity in hHOs. To evaluate this finding, we performed immunofluorescence analysis for secondary cardiac cell lineages. Confocal imaging confirmed the presence of cardiac fibroblasts positive for THY1 and VIM (Fig. 5a), which made up $12 \pm 2\%$ of the tissues in the hHOs (Fig. 5e), similar to the composition of the fetal heart described in the literature¹⁸. Further confocal imaging revealed a robust interconnected network of endothelial cells (PECAM1⁺), and vessel-like formation throughout the organoid (Fig. 5b). Higher magnification images uncovered a complex web of endothelial cells adjacent to or embedded into myocardial tissue (Fig. 5c, **Suppl. Video 4**). 3D reconstruction of confocal imaging stacks showed a well-connected endothelial network intertwined in the hHO tissue (**Suppl. Videos 4 & 5**). These results strongly indicate that during hHO development, self-organizing endothelial vascular networks emerge in response to the 3D cardiovascular environment, adding a coronary-like vascular network to the organoids (a phenomenon not observed before). We also observed chamber-like areas within the TNNT2⁺ and suspected they might possess chamber-like qualities and mimic early heart chamber formation. Immunofluorescence analysis for the endocardial marker NFATC1 revealed the formation of an endocardial layer of NFATC1⁺ cells lining these spaces, similar to the endocardial lining of the heart (Fig. 5d). Figure 5e shows a quantification of the contribution of these different cell populations to the organoids. Next, we employed optical coherence tomography (OCT) to characterize chamber properties using minimally invasive means, thus preserving chamber physical and morphological properties. OCT showed clear chamber spaces within the hHOs, typically with one or two large chambers near the center of the organoids (Fig. 6a, **Suppl. Figure 4a-c**). 3D reconstruction of the internal hHO topology revealed a high degree of interconnectivity between these chambers (**Suppl. Videos 6–8**). The presence of chambers was further confirmed using light-sheet imaging of whole organoids (Fig. 6b). Given the relatively large size of our heart organoids (up to 1 mm), we decided to verify whether the formation of these chambers could be associated to internal cell death. To do this, we created a transgenic hiPSC line expressing FlipGFP, a non-fluorescent engineered GFP variant which turns fluorescent upon effector caspase activation and is thus a reporter for apoptosis¹⁹. FlipGFP organoids in control conditions exhibited no fluorescence indicating that there is no significant programmed cell death (**Suppl. Figure 4d**). This observation is further supported by the lack of internal cellular debris observed during confocal imaging (data not shown). Doxorubicin-treated hHOs were used as a positive control for apoptosis (**Suppl. Figure 4d**), with evident signs of cell death.

Ultrastructural analysis of hHOs showed features similar to those typically found in age-matched human fetal hearts, with well-defined sarcomeres surrounded by mitochondria, and containing gap junctions and T-tubules (Fig. 6c). We also measured electrophysiological activity to determine functionality. We utilized

an in-house multi-electrode array sensor technology develop (**Suppl. Figure 5**) to show that hHOs exhibit normal electrophysiological activity with well-defined QRS complexes and T and P waves, and regular action potentials (Fig. 6d).

BMP4 and activin A improve heart organoid chamber formation and vascularization. The growth factors bone morphogenetic protein 4 (BMP4) and activin A have frequently been used as alternatives to small molecule Wnt signaling manipulation since they are the endogenous morphogens that pattern the early embryonic cardiogenic mesoderm and determine heart field specification *in vivo*^{20,21}. We suspected that BMP4 and activin A, in combination with our small molecule Wnt activation/inhibition protocol, could synergistically improve the ability of hHOs to recapitulate cardiac development *in vitro*. We tested the effect of BMP4 and activin A in the context of our optimized protocol by adding the two morphogens at 1.25 ng/ml and 1 ng/ml, respectively (recommended concentrations found in the literature²⁰), at differentiation day 0 in conjunction with 4 μ M CHIR99021. No significant differences were found in formation of myocardial (TNNT2+) or epicardial (WT1+/TJP1+) tissue between control and treated hHOs (Fig. 7a). However, significant differences in organoid size were observed as hHOs treated with growth factors were about 15% larger in diameter (Fig. 7b, c). This difference may correspond with the increase in microchamber number and connectivity, as BMP4/Activin A-treated hHOs had more microchambers that were ~ 50% more interconnected with other chambers compared to control hHOs (Fig. 7d, e, g). Immunofluorescence and confocal analysis of organoids treated with BMP4 and activin A showed a 400% increase in the area of PECAM1 + tissue, indicating a significant effect on organoid vascularization (Fig. 7f, h), which might also account for the increase in hHO size.

Modeling DDP-induced CHD using human heart organoids. As proof-of-concept on the utility of our system, we decided to use our hHO model to study the effects of diabetes during pregnancy on cardiac development. Diabetes affects a large number of the female population in reproductive age and there is significant epidemiological evidence linking diabetes during the first trimester of pregnancy to increased risk of CHD (up to 12% in some cases, a 12-fold increase)²², but little understanding of the underlying mechanisms. To do this, we first modified hHO culture conditions to reflect reported normal physiological levels of glucose and insulin (3.5 mM glucose, 170 pM insulin, NHOs)²³ and reported diabetic conditions (11.1 mM glucose and 58 nM insulin, DDPHOs)^{23,24}. Interestingly, normal conditions also differed from the original protocol's glycemic and insulin conditions (due to most media being originally developed for cancer cell culture and containing abnormally high levels of glucose). NHOs developed at a slower pace than their higher glucose counterparts but presented better physical organization, with formation of heart tube-like structures and later segmentation into different well-defined areas reminiscent of heart looping and chamber formation (**Suppl. Figure 6a**) without evidence of cell death or abnormal physiology (Fig. 8 **and data not shown**). However, their structure was also significantly more delicate and could easily be damaged (Fig. 8a). NHOs and DDPHOs showed significant morphological differences as early as day 4 of differentiation. NHOs were slower to grow and exhibited patterning and elongation between days 4 and 8, while DDPHOs remained spherical throughout the two-week period (Fig. 8a). DDPHOs were also significantly larger in size after 1 week of differentiation (Fig. 8b), suggesting hypertrophy, a common

outcome of diabetes in newborns, which typically suffer from macrosomia in all organs. Electrophysiology analysis showed increased amplitude and frequency in action potentials in DDPHOs (Fig. 8c and **Suppl. Figure 6b, c and d**) suggesting higher activity in the diabetic organoids. Metabolic assays for glycolysis and oxygen consumption revealed decreased oxygen consumption rate in DDPHOs and increased glycolysis when compared to NHOs (Fig. 8d, e and **Suppl. Figure 6e**). TEM imaging revealed DDPHOs had a reduced number of mitochondria surrounding sarcomeres (Fig. 8f) and a significantly larger number of lipid droplets, suggesting dysfunctional lipid metabolism. None of these phenotypes were found in NHOs. Confocal microscopy of myocardial and epicardial markers revealed a drastic difference in morphological organization as DDPHOs contained epicardial tissue surrounded by myocardial tissue, whereas NHOs contained epicardial tissue on top of or beside myocardial tissue as expected (Fig. 8g). Furthermore, compared with normal glycemia conditions, diabetic hHOs showed decreased MYL2⁺ ventricular cardiomyocytes and enlarged chambers, again suggesting a dilated cardiomyopathy-like phenotype (Fig. 8h). These differences in impaired structural/developmental organization and lipid metabolism in DDPHOs are consistent with expected phenotypes found in diabetic patients and newborns exposed to high glucose/insulin. Taken together, our data suggest significant molecular and metabolic perturbations between NHOs and DDPHOs consistent with previous studies on DDP suggesting increased oxidative stress, cardiomyopathy and altered lipid profiles²⁵⁻²⁷, and constitute a significant step forward to model metabolic disorders in human organoids.

Discussion

In recent years, hPSC-derived cardiomyocytes have become critically useful tools to model aspects of heart development^{12,28,29}, human genetic cardiac disease³⁰⁻³³, therapeutic screening^{34,35}, and cardiotoxicity testing³⁶⁻³⁹. Nonetheless, the complex structural morphology and multitude of tissue types present in the human heart impose severe limitations to current *in vitro* models. Previous attempts at generating three-dimensional cardiac tissues typically include cardiomyocytes and only one or two other cardiac cell lineages⁴⁰⁻⁴². Here we sought to create a highly reproducible, scalable, and novel differentiation protocol that yields physiologically relevant human heart organoids with high structural and multicell type complexity using hPSCs. We created and optimized multistep manipulation conditions for canonical Wnt signaling using GSK3 and *PORCN* inhibitors. These conditions lead to the formation of most cardiac lineages in a self-assembling heart organoid with similar properties to the fetal heart. This method consistently yields cardiac organoids comprised of approximately 59% cardiomyocytes, 15% epicardial cells, 13% endocardial cells, 12% cardiac fibroblasts, and 1% endothelial cells (by area) and shows robust beating throughout the entire structure within a week from differentiation initiation. The organization and specification of these cell types are likely controlled at least in part through HAND transcription factor expression, as HAND1 and HAND2 lineage-derived cells contribute to the developing myocardium, epicardium, endocardium, and vasculature^{16,43-45}. The fact that both FHF and SHF HAND markers are present suggests that they play a role in the development of the structural and cell type complexity seen in our hHOs. Notably, hHOs were successfully derived from three independent iPSC lines and one ESC line, demonstrating reproducibility. The fetal-like morphology of the cardiomyocytes and the

self-assembling nature of the hHOs allude to a complex three-dimensional structure containing a multitude of cardiac cell lineages allowing for higher-order interactions between different heart tissues. When compared with existing cardiomyocyte monolayer differentiation methods, hHOs showed higher expression of genes associated with conduction, contractile function, calcium handling, and various cardiac cell populations, which better resembles gene expression data retrieved from human fetal hearts. The depiction of a complex transcriptome highly recapitulative of human fetal heart tissue further strengthens the complexity and validity of the hHO as a model of human heart development.

The epicardium, an epithelial layer that encapsulates the human heart, is involved in many important heart processes, including heart development, metabolism, lipid homeostasis, and myocardial injury responses^{46,47}. Epicardial signaling cascades are essential for cardiac lineage specification⁴⁶. During embryonic development, cells from the proepicardial organ (PEO), an extra-cardiac cluster of embryonic cells⁴⁷, migrate to the surface of the heart to form the epicardium. Some of these cells can undergo EMT to generate other cardiac lineages including cardiac fibroblasts^{15,46-48}. Due to its capacity to communicate with the myocardium and its ability to mobilize stem cell populations, the epicardium has become a key focus of research in cardiac regeneration and repair^{11,46,47}. The epicardium also plays a fundamental but underexplored role in multiple types of cardiovascular and metabolic disease, including diabetic cardiomyopathy, coronary artery disease, and metabolic syndrome. In this last condition, epicardial-derived fat experiences a significant expansion and correlates strongly with morbidity, highlighting the potential relevance of the epicardium to human disease. Inspired by a previous epicardial differentiation method¹¹, we created and optimized conditions for producing heart organoids with well-defined regions of epicardial tissue adjacent to myocardial tissue. These epicardial-myocardial interactions are important in mammalian heart development and function as epicardial cells increase cardiomyocyte growth in 3D engineered heart tissues (EHTs) and co-transplantation of both cell types into rat hearts increases endothelial cell production⁴². Our hHO protocol will facilitate the study and modeling of physiologically relevant epicardial-myocardial interactions *in vitro*.

The important role that cardiac fibroblasts play on cardiac development and cardiac matrix production/organization is often overlooked in *in vitro* models. Most cardiac fibroblasts in embryonic development arise from the PEO^{15,49,50}, highlighting the necessity of epicardial induction in developmental heart models. These fibroblasts facilitate cardiomyocyte functionality in hPSC-derived 3D cardiac microtissues, and as such, their inclusion in any *in vitro* human heart model is paramount⁴⁰. Immunofluorescence analysis of our hHOs revealed the presence of cardiac fibroblast markers including the membrane glycoprotein Thy1, which is involved in cell-cell and cell-matrix adhesion^{50,51}, and the intermediate filament protein Vimentin, typically seen in cells of mesenchymal lineage⁵¹. Other cardiac fibroblast markers were found in the hHOs via RNA-sequencing analysis, including DDR2 which plays an important role in EMT⁵⁰, and the FHF marker PDGFR α which is also crucial for vascularization during development⁵¹. These data provide a strong indication of the increased complexity of our hHO system and its close resemblance to fetal heart tissue.

An acute limitation of many organoid systems is a lack of a functional vascular network to facilitate the exchange of nutrients and removal of waste material, as they instead rely solely on diffusion^{4,52,53}. Several vascularized organoids have been described in the literature modeling the brain⁴, kidney⁵⁴, and blood vessel⁵⁵, however, none have been described in cardiac organoids. In these studies, various techniques are used to induce vascularization including implantations in mice⁴, culturing the organoids under flow⁵⁴, and embedding endothelial cells in a Matrigel/collagen matrix and inducing their migration⁵⁵ to create a vascular network. Remarkably, we observed the formation of a robust interconnected vascular plexus in our final protocol for hHOs without any additional steps. Further studies into the functionality of this vascular tissue will be necessary, particularly to determine the maturity of the vessels, and if they closely resemble coronary vasculature. This latter feature would open the door to modeling coronary vasculature pathologies that arise due to CVD and metabolic disorders.

In addition to vasculature, we also observed spontaneous hHO reorganization into interconnected chambers, a powerful 3D feature indicative of recapitulation of fetal-like organogenesis. Previous studies of microchamber formation *in vitro* utilized micropatterning of hPSCs into a confined area to generate 3D cardiac microchambers with cell-free regions, a myofibroblast perimeter, and nascent trabeculae⁵⁶. Other reports have produced 3D bio-printed hPSC-laden scaffolds and differentiated them to beating cardiac microtissues with two chambers⁵⁷. While the structures generated in these studies showed some fetal-like formation of cardiac microchambers, they lacked endocardial tissue¹⁰, a crucial player in heart maturation and morphogenesis⁵⁸. The hHOs reported here form multiple microchambers lined with NFATC1 + endocardial cells which are interconnected as seen in the OCT cross-sectional imaging (**Suppl. Videos 6–8**). Expression of specific ECM genes in the hHOs resembling the fetal heart matrix, such as *COL1A1*, *COL4A1*, *COL5A2*, *FBN1*, *EMILIN1*, *HSPG2*, and *LAMA2* (**Suppl. Figure 3d**) might be an important factor in chamber organization, as ECM components have been shown to mediate the formation of chambered mouse cardiac organoids⁵⁹. Therefore, the expression of these genes in our hHOs deserves further examination in the future. The microchambers may also specify further into atrial-like and ventricular-like regions, as cardiomyocytes from both lineages are seen in separate regions in our hHOs.

Together with the use of small-molecule inhibitors that manipulate canonical Wnt signaling pathways, successful cardiomyocyte differentiation has been achieved in the past using morphogens such as BMP4 and activin A^{7,12}. These growth factors lead to the induction of cardiac mesoderm in the embryo⁶⁰ and established differentiation protocols using them show effective differentiation to various cardiac mesoderm progenitors^{8,60,61}. Recently, gradient exposures to specific concentrations of BMP4 and activin A have been studied in the specification of first and second heart field formation²⁰. The addition of these growth factors to the initial CHIR exposure in our hHO differentiation protocol led to improved morphological features such as increased microchamber interconnectivity and vascularization.

In the past few years, 3D human cardiac tissues have been used to model genetic and non-genetic conditions (myocardial infarction, drug cardiotoxicity)^{62,63}. We have provided evidence here that our hHOs can be valuable models to study CHD in diabetes during pregnancy, a significant understudied

medical problem. Maternal diabetes is one of the most common causes of newborn CHD (up to 12% of newborns from diabetic mothers have some form of CHD²²). Using healthy and diabetic levels of glucose and insulin in the differentiation media, we demonstrate the effects of diabetic conditions on the developmental process of hHOs. Organoids developing in healthy conditions displayed active structural changes including patterning, while hHOs in diabetic conditions developed larger and spherical. This finding may hint towards an effect on the ability of the early heart to properly form the heart tube, leading to malformations of the heart as it loops into four chambers. Furthermore, the larger size of the diabetic hHOs suggests an early sign of cardiac hypertrophy, a hallmark of maternal DDP⁶⁴. The apparent reduction in mitochondria, dysfunctional lipid metabolism, and impaired structural organization of key tissue types hint towards unraveling the pathogenesis of CHD in diabetes during pregnancy. Future studies will utilize this organoid differentiation protocol to explore these dysfunctions and malformations and conduct high throughput screening for potential targets for remedies. In summary, we describe here a highly reproducible and high-throughput human heart organoid derivation method, with multicell type and morphological complexity closely recapitulating that of the developing human fetal heart. This model constitutes a valuable tool to investigate the development of the human heart and the etiology of congenital heart defects. Furthermore, refinement and improved maturation protocols might allow us to model adult cardiac settings, such as cardiotoxicity screening and cardiovascular-related disorders.

Materials And Methods

Ethics statement. All human stem cell procedures were approved by MSU's Institutional Stem Cell Research Committee.

Stem cell culture. Human iPSC lines used in this study were iPSC-L1, AICS-0037-172 (Coriell Institute for Medical Research, alias AICS), iPSCORE_16_3 (WiCell, alias iPSC-16) and human ESC line H9. All PSC lines were validated for pluripotency and genomic integrity. hPSCs were cultured in Essential 8 Flex medium containing 1% penicillin/streptomycin (Gibco) on 6-well plates coated with growth factor-reduced Matrigel (Corning) in an incubator at 37°C, 5% CO₂, until 60-80% confluency was reached, at which point cells were split into new wells using ReLeSR passaging reagent (Stem Cell Technologies).

PSC monolayer cardiac differentiation. Differentiation was performed using the small molecule Wnt modulation strategy as previously described⁷, (referred to as monolayer 1 in the text), with small modifications. Briefly, differentiating cells were maintained in RPMI with B27 minus insulin from day 0-7 of differentiation and maintained in RPMI with B27 supplement (Thermo) from day 7-15 of differentiation. Cells were treated with 10 uM GSK inhibitor CHIR99021 (Selleck) for 24 hours on day 0 of differentiation and with 2 uM PORCN inhibitor, Wnt-C59 (Selleck), for 48 hours from day 3-5 of differentiation. The alternative differentiation protocol (referred to as monolayer 2) was described in Bertero et al, 2019¹⁴.

Self-assembling human heart organoid differentiation. Accutase (Innovative Cell Technologies) was used to dissociate PSCs for spheroid formation. After dissociation, cells were centrifuged at 300 g for 5

minutes and resuspended in Essential 8 Flex medium containing 2 μM ROCK inhibitor Thiazovivin (Millipore Sigma). hPSCs were then counted using a Moxi Cell Counter (Orflo Technologies) and seeded at 10,000 cells/well in round bottom ultra-low attachment 96-well plates (Costar) on day -2. The plate was then centrifuged at 100 g for 3 minutes and placed in an incubator at 37°C, 5% CO₂. After 24 hours (day -1), 50 μl of media was carefully removed from each well and 200 μl of fresh Essential 8 Flex medium was added for a final volume of 250 μl /well. The plate was returned to the incubator for a further 24 hours. On day 0, 166 μl (~2/3 of total well volume) of media was removed from each well and 166 μl of RPMI 1640/B-27, minus insulin (Gibco) containing CHIR99021 (Selleck) was added at a final concentration of 4 μM /well along with BMP4 at 0.36 pM (1.25ng/ml) and ActA at 0.08 pM (1ng/ml) for 24 hours. On day 1, 166 μl of media was removed and replaced with fresh RPMI1640/B-27, minus insulin. On day 2, RPMI/B-27, minus insulin containing Wnt-C59 (Selleck) was added for a final concentration of 2 μM Wnt-C59 and the samples were incubated for 48 hours. The media was changed on day 4 and day 6. On day 6, media was changed to RPMI1640/B-27 (Gibco). On day 7, a second 4 μM CHIR99021 exposure was conducted for 1 hour in RPMI1640/B-27. Subsequently, media was changed every 48 hours until organoids were ready for analysis. Diabetic conditions were simulated by using basal RPMI media with 11.1 mM glucose and 58 nM insulin and compared with control media containing 3.5 mM glucose and 170 pM insulin.

Lentiviral transduction. FlipGFP plasmid (Vector Builder) was transduced into L1 iPSC line using ZymoPURE II Plasmid Midiprep Kit (Fisher Scientific), according to manufacturer instructions. HEK293t were cultured in D10 media (DMEM + 10% FBS + 1% P/S), and later switched with reduced serum OptiMem (Gibco, Fisher Scientific), for 1 hour. Lipofectamine mixture (100 μl Lipofectamine 2000 (Thermo Fisher) + 4 ml OptiMem sitting at room temperature for 5 minutes) was mixed with Plus reagent mixture (200 μl Plus reagent (Invitrogen, Fisher Scientific) + 4 ml OptiMem + 20 μg lentiCRISPR plasmid + 10 μg pMD2.gpVSVg (or pVSVgpMD2.g) + 15 μg psPAX2) and were then added to the HEK293t cells and allowed to incubate at 37°C for 6 hours. Following this, the media was changed to 30 ml D10 + 1% BSA per flask, without antibiotics. After 48-60 hours, the media was collected and centrifuged at 3,000 rpm at 4°C for 10 minutes. The supernatant was transferred to an Amicon Filter Unit (Millipore-Sigma) and spun in a tabletop centrifuge at 3200g for 30 minutes at 4°C. The flow through was dumped and the process was repeated. The concentrated virus was aliquoted and stored at -80°C. Virus aliquot and polybrene (Fisher Scientific) were thawed at 37°C. Virus and polybrene were delivered to iPSC-L1s at low to mid confluences and incubated overnight. The next morning, the media was changed, and cells rested for 24 hours. Puromycin was added to the wells and selection was maintained for ~3-5 days. Surviving clones were collected, replated, and expanded.

Immunofluorescence. hHOs were transferred to microcentrifuge tubes (Eppendorf) using a cut 1000- μL pipette tip to avoid disruption to the organoids and fixed in 4% paraformaldehyde solution (dissolved in phosphate buffered saline (PBS)) for 30 minutes at room temperature. Fixation was followed by 3 washes in PBS-Glycine (20 mM) and incubation in blocking/permeabilization solution (10% Donkey Normal Serum, 0.5% Triton X-100, 0.5% bovine serum albumin (BSA) in PBS) on a thermal mixer (Thermo

Scientific) at 300 RPM at 4°C overnight. hHOs were then washed 3 times in PBS and incubated with primary antibodies (**Supp. Table 2**) in Antibody Solution (1% Donkey Normal Serum, 0.5% Triton X-100, 0.5% BSA in PBS) on a thermal mixer at 300 RPM at 4°C for 24 hours. Primary antibody exposure was followed by 3 washes in PBS and incubation with secondary antibodies (**Supp. Table 2**) in Antibody Solution on a thermal mixer at 300 RPM at 4°C for 24 hours in the dark. The stained hHOs were washed 3 times in PBS before being mounted on glass microscope slides (Fisher Scientific) using Vectashield Vibrance Antifade Mounting Medium (Vector Laboratories). 90 µm Polybead Microspheres (Polyscience, Inc.) were placed between the slide and the coverslip (No. 1.5) to preserve some of the 3D structure of the organoids while accommodating the penetration capacity of the confocal microscope.

Confocal microscopy and image analysis. Samples were imaged using two confocal laser scanning microscopes (Nikon Instruments A1 Confocal Laser Microscope; Zeiss LSM 880 NLO Confocal Microscope System) and images were analyzed using Fiji (<https://imagej.net/Fiji>). For tissue region quantification in the organoids, DAPI positive cells were used for normalization against the target cell marker of interest across three z-planes throughout each organoid. A MaxEntropy threshold was used to measure the PECAM1+ tissue, discarding any stained region that took up less than 25 µm² to remove noise.

RNA sequencing and transcriptomic analysis. RNA was extracted at 11 different time points throughout the hHO fabrication and differentiation protocol shown in **Figure 2a**. The time points are as follows: days 0, 1, 3, 5, 7, 9, 11, 13, 15, 17, and 19. At each time point, eight organoids were removed and stored in RNAlater (Qiagen) at -20°C until all samples were collected. RNA was extracted using the Qiagen RNEasy Mini Kit according to manufacturer instructions (Qiagen, 74104), and the amount of RNA was measured using a Qubit Fluorometer (Thermo). RNA samples were sent to the MSU Genomics Core where the quality of the samples was tested using an Agilent 2100 Bioanalyzer followed by RNA sequencing using an Illumina HiSeq 4000 system. For RNA-seq sample processing a pipeline was created in Galaxy. Briefly, sample run quality was assessed with FASTQC, and alignment to hg38 was carried out using HISAT2. Counts were obtained using featureCounts and differential expression analysis was performed with EdgeR. Further downstream bioinformatic analysis were performed in Phantasus 1.5.1 (artyomovlab.wustl.edu/phantasus) and ToppGene.

Optical coherence tomography analysis. A customized spectral-domain OCT (SD-OCT) system was developed to acquire 3D images of the cardiac organoids. As shown in **Suppl. Fig. 7**, a superluminescent diode (SLD 1325, Thorlabs) was used as the light source to provide broadband illumination with a central wavelength of 1320nm and spectral range of 110 nm. The output of the SLD was split 50/50 with a fiber coupler and transmitted to the sample and reference arms, respectively. A galvanometer (GVSM002-EC/M, Thorlabs) was used to scan the optical beam in transverse directions on the sample. The SD-OCT setup used a custom-designed spectrometer consisting of a 1024-pixel line scan camera (SU1024-LDH2, Sensors Unlimited), a 1145-line pairs per mm diffraction grating (HD 1145-line pairs per mm at 1310 nm, Wasatch Photonics) and an f = 100 mm F-theta lens (FTH100-1064, Thorlabs). The sensitivity of the OCT system was measured as ~104 dB when operating at 20 kHz A-scan rate. The axial resolution of the SD-

OCT system was measured to be ~7 mm in tissue. A 5X objective lens (5X Plan Apo NIR, Mitutoyo) was used to achieve a transverse image resolution of ~7 mm, and the scanning range used for the cardiac organoids imaging was ~2 mm X 2 mm. hHOs were placed into a 96-well plate with PBS, and imaged at 20-kHz A-scan rate. Obtained OCT datasets of the cardiac organoids were first processed to generate OCT images with corrected scales. Then OCT images were further de-noised using a speckle-modulation generative adversarial network⁷⁰ to reduce the speckle noise. 3D renderings of OCT images were performed using Amira software (Thermo Fisher Scientific).

Light-sheet imaging and analysis. A customized high-speed, axially swept light sheet fluorescence microscope developed in-house was used. The microscope has 3 built-in laser channels (405nm, 488nm and 561nm) and FOV of 832 x 832 um, with two custom-made multi-immersion high NA objective lenses (16x magnification, ASI) and a sCMOS camera (Andor Zyla 4.2). Fixed organoid imaging was achieved by placing the sample in a plate dish and securing it with double-sided tape (3M). The organoid was then submerged into the water. An ASI control stage brings the organoid sample into the light sheet focus plane and submerges the two-objective lens under the water to match the refraction index for imaging. Scanning was performed with the ASI control box with a scanning step size was set to 1um. 3 identical scans with different laser channel were applied to a single organoid. After capture, fluorescence images were processed using ImageJ.

TEM sample preparation and imaging. Organoids were fixed in 4% PFA for 30 minutes followed by 3 washes in water, 10 minutes each. Post fixation was performed in 1% osmium tetroxide in cacodylate buffer (pH 7.3) for 60 minutes at room temperature. Organoids were embedded in 2% agarose in water, solidified using ice, for manipulation. Then, serial dilution of acetone was used for dehydration (25%, 50%, 75%, 90% and 3 times in 100%) for 10 minutes each. Organoids were infiltrated with Spurr resin (Electron Microscopy Sciences) by immersion in 1:3, 2:2 and 3:1 solutions of resin in acetone, 3 hours each under agitation, following embedding in 100% resin for 24 hours, and polymerization at 60°C overnight. Ultra-thin sections (50-70 nm) were cut using RMC PTXL Leica Ultramicrotome and collected in carbon coated copper grids 200 mesh. Before observation, all samples were positively stained in 2% uranyl acetate and 1% lead citrate for 6 and 3 minutes, respectively. The grids were examined at 100 keV using a JEOL 1400 Flash transmission electron microscope.

Electrophysiology. An in-house microelectrode array (MEA) system described previously⁶⁵ was used to record electrical activity of individual organoids. Live organoids were placed on the MEA inside a PDMS well in culture media supplemented with 15 mM HEPES. The MEA was placed within a Faraday cage inside an incubator at 37°C at low humidity to avoid damage to the MEA system. Each organoid was recorded for a period of 30 minutes, and the PDMS well was washed with PBS between organoids.

Seahorse metabolic analysis. A Seahorse XFp analyzer (Agilent) was used to conduct a glycolysis rate assay as per manufacturer instructions. Three organoids per condition were dissociated separately using STEMdiff™ Cardiomyocyte Dissociation Kit (Stem Cell Technologies), in each assay.

Data Availability. All organoid data sets shown in this study are available at the National Center for Biotechnology Information Gene Expression Omnibus repository under accession number GSE153185. RNA-seq data from monolayer differentiation method 2 and fetal heart were obtained from GSE106690⁴³. All other data generated and/or analysed during this study is included in the published article and its supplementary information files.

Code availability. No code was developed in this article.

Statistical analyses. All analyses were performed using Excel or GraphPad software. All data presented a normal distribution. Statistical significance was evaluated with a standard unpaired Student t-test (2-tailed; $P < 0.05$) when appropriate. For multiple-comparison analysis, 1-way ANOVA with the Tukey's or Dunnett's post-test correction was applied when appropriate ($P < 0.05$). All data are presented as mean \pm SD and represent a minimum of 3 independent experiments with at least 3 technical replicates unless otherwise stated.

Declarations

Acknowledgments

We wish to thank the MSU Advanced Microscopy Core and Dr. William Jackson at the MSU Department of Pharmacology and Toxicology for access to confocal microscopes, and the MSU Genomics Core for sequencing services. We also wish to thank all members of the Aguirre Lab for valuable comments and advice.

Author contributions

YLI and AA designed all experiments and conceptualized the work. YLI performed all experiments and data analysis. MG performed cell and organoid culture. AHW performed cell and organoid culture and confocal imaging. KB performed cell culture. BV created cell lines for apoptosis analysis. WY and WL designed the electrophysiological instruments, conducted electrophysiology recordings and data analysis. BL and ZQ performed all light-sheet imaging and data analysis. JZ, GN and CZ performed optical coherence tomography experiments and data analysis. NP and XC performed TEM sample preparation and imaging. YLI, AHW and AA wrote the manuscript.

Sources of Funding

Work in Dr Aguirre's laboratory was supported by the National Heart, Lung, and Blood Institute of the National Institutes of Health under award number K01HL135464 and by the American Heart Association under award number 19IPL0134660342. Work in Dr. Zhou's laboratory was supported by grants from the National Institutes of Health under award number R01EB025209. Work in Dr. Li's laboratory was supported in part by the National Science Foundation under award number ECCS-2024270 and Michigan State University Graduate Excellence Fellowship.

Disclosures

The authors declare no conflicts of interest.

References

1. Takasato, M. *et al.* Kidney organoids from human iPS cells contain multiple lineages and model human nephrogenesis. *Nature* **526**, 564–568 (2015).
2. Crespo, M. *et al.* Colonic organoids derived from human induced pluripotent stem cells for modeling colorectal cancer and drug testing. *Nat. Med.* **23**, 878–884 (2017).
3. Serra, D. *et al.* Self-organization and symmetry breaking in intestinal organoid development. *Nature* **569**, 66–72 (2019).
4. Mansour, A. A. *et al.* An in vivo model of functional and vascularized human brain organoids. *Nat. Biotechnol.* **36**, 432–441 (2018).
5. Dunn, K. K. & Palecek, S. P. Engineering scalable manufacturing of high-quality stem cell-derived cardiomyocytes for cardiac tissue repair. *Front. Med.* **5**, (2018).
6. Burridge, P. W. *et al.* Chemically defined generation of human cardiomyocytes. *Nat. Methods* **11**, 855–860 (2014).
7. Lian, X. *et al.* Directed cardiomyocyte differentiation from human pluripotent stem cells by modulating Wnt/ β -catenin signaling under fully defined conditions. *Nat. Protoc.* **8**, 162–175 (2013).
8. Breckwoldt, K. *et al.* Differentiation of cardiomyocytes and generation of human engineered heart tissue. *Nat. Protoc.* **12**, 1177–1197 (2017).
9. Giacomelli, E., Mummery, C. L. & Bellin, M. Human heart disease: lessons from human pluripotent stem cell-derived cardiomyocytes. *Cell. Mol. Life Sci.* **74**, 3711–3739 (2017).
10. Hoang, P., Wang, J., Conklin, B. R., Healy, K. E. & Ma, Z. Generation of spatial-patterned early-developing cardiac organoids using human pluripotent stem cells. *Nat. Protoc.* **13**, 723–737 (2018).
11. Bao, X. *et al.* Long-term self-renewing human epicardial cells generated from pluripotent stem cells under defined xeno-free conditions. *Nat. Biomed. Eng.* **1**, 1–12 (2017).
12. Lian, X. *et al.* Robust cardiomyocyte differentiation from human pluripotent stem cells via temporal modulation of canonical Wnt signaling. *Proc. Natl. Acad. Sci. U. S. A.* **109**, (2012).
13. Lian, X. *et al.* Chemically defined, albumin-free human cardiomyocyte generation. *Nat. Methods* **12**, 595–596 (2015).
14. Bertero, A. *et al.* Dynamics of genome reorganization during human cardiogenesis reveal an RBM20-dependent splicing factory. *Nat. Commun.* **10**, 1538 (2019).
15. Brade, T., Pane, L. S., Moretti, A., Chien, K. R. & Laugwitz, K. L. Embryonic heart progenitors and cardiogenesis. *Cold Spring Harb. Perspect. Med.* **3**, 1–18 (2013).
16. George, R. M. & Firulli, A. B. Hand Factors in Cardiac Development. *Anat. Rec.* **302**, 101–107 (2019).

17. Kelly, R. G., Buckingham, M. E. & Moorman, A. F. Heart fields and cardiac morphogenesis. *Cold Spring Harb. Perspect. Med.* **4**, 1–11 (2014).
18. Pinto, A. R. *et al.* Revisiting Cardiac Cellular Composition Alexander. *Circ Res.* **118**, 400–409 (2017).
19. Zhang, Q. *et al.* Designing a Green Fluorogenic Protease Reporter by Flipping a Beta Strand of GFP for Imaging Apoptosis in Animals. *J. Am. Chem. Soc.* **141**, 4526–4530 (2019).
20. Andersen, P. *et al.* Precardiac organoids form two heart fields via Bmp/Wnt signaling. *Nat. Commun.* **9**, (2018).
21. Sa, S. & McCloskey, K. E. Activin A and BMP4 signaling for efficient cardiac differentiation of H7 and H9 human embryonic stem cells. *J. Stem Cells Regen. Med.* **8**, 198–202 (2012).
22. Narchi, H. & Kulaylat, N. Heart disease in infants of diabetic mothers. *Images Paediatr. Cardiol.* **2**, 17–23 (2000).
23. Güemes, M., Rahman, S. A. & Hussain, K. What is a normal blood glucose? *Arch. Dis. Child.* **101**, 569–574 (2016).
24. Diagnosis and Classification of Diabetes Mellitus. *Diabetes Care* **32**, S62–S67 (2009).
25. Moazzen, H. *et al.* N-Acetylcysteine prevents congenital heart defects induced by pregestational diabetes. 1–13 (2014).
26. Giacco, F. & Brownlee, M. Oxidative stress and diabetic complications. *Circ. Res.* **107**, 1058–1070 (2010).
27. Wu, Y. *et al.* Type 2 diabetes mellitus induces congenital heart defects in murine embryos by increasing oxidative stress, endoplasmic reticulum stress, and apoptosis. *Am. J. Obstet. Gynecol.* **215**, 366.e1-366.e10 (2016).
28. Ronaldson-Bouchard, K. *et al.* Advanced maturation of human cardiac tissue grown from pluripotent stem cells. *Nature* **556**, 239–243 (2018).
29. Yang, X. *et al.* Fatty Acids Enhance the Maturation of Cardiomyocytes Derived from Human Pluripotent Stem Cells. *Stem Cell Reports* **13**, 657–668 (2019).
30. Sun, N. *et al.* Patient-specific induced pluripotent stem cells as a model for familial dilated cardiomyopathy. *Sci. Transl. Med.* **4**, (2012).
31. Hashem, S. I. *et al.* Brief report: Oxidative stress mediates cardiomyocyte apoptosis in a human model of danon disease and heart failure. *Stem Cells* **33**, 2343–2350 (2015).
32. Panopoulos, A. D. *et al.* iPSCORE: A Resource of 222 iPSC Lines Enabling Functional Characterization of Genetic Variation across a Variety of Cell Types. *Stem Cell Reports* **8**, 1086–1100 (2017).
33. Stroud, M. J. *et al.* Luma is not essential for murine cardiac development and function. *Cardiovasc. Res.* **114**, 378–388 (2018).
34. Liang, P. *et al.* Drug screening using a library of human induced pluripotent stem cell-derived cardiomyocytes reveals disease-specific patterns of cardiotoxicity. *Circulation* **127**, 1677–1691 (2013).

35. Mills, R. J. *et al.* Functional screening in human cardiac organoids reveals a metabolic mechanism for cardiomyocyte cell cycle arrest. *Proc. Natl. Acad. Sci. U. S. A.* **114**, E8372–E8381 (2017).
36. Osataphan, N., Phrommintikul, A., Chattipakorn, S. C. & Chattipakorn, N. Effects of doxorubicin-induced cardiotoxicity on cardiac mitochondrial dynamics and mitochondrial function: Insights for future interventions. *J. Cell. Mol. Med.* 1–24 (2020) doi:10.1111/jcmm.15305.
37. Braam, S. R. *et al.* Prediction of drug-induced cardiotoxicity using human embryonic stem cell-derived cardiomyocytes. *Stem Cell Res.* **4**, 107–116 (2010).
38. Burridge, P. W. *et al.* Human induced pluripotent stem cell–derived cardiomyocytes recapitulate the predilection of breast cancer patients to doxorubicin-induced cardiotoxicity. *Nat. Med.* **22**, 547–556 (2016).
39. Kitani, T. *et al.* Human-Induced Pluripotent Stem Cell Model of Trastuzumab-Induced Cardiac Dysfunction in Patients With Breast Cancer. *Circulation* **139**, 2451–2465 (2019).
40. Giacomelli, E. *et al.* Human-iPSC-Derived Cardiac Stromal Cells Enhance Maturation in 3D Cardiac Microtissues and Reveal Non-cardiomyocyte Contributions to Heart Disease. *Cell Stem Cell* **26**, 862–879.e11 (2020).
41. Giacomelli, E. *et al.* Three-dimensional cardiac microtissues composed of cardiomyocytes and endothelial cells co-differentiated from human pluripotent stem cells. *Development* **144**, 1008–1017 (2017).
42. Bargehr, J. *et al.* Epicardial cells derived from human embryonic stem cells augment cardiomyocyte-driven heart regeneration. *Nat. Biotechnol.* **37**, 895–906 (2019).
43. Barnes, R. M., Firulli, B. A., Conway, S. J., Vincentz, J. W. & Firulli, A. B. Analysis of the Hand1 cell lineage reveals novel contributions to cardiovascular, neural crest, extra-embryonic, and lateral mesoderm derivatives. *Dev. Dyn.* **239**, 3086–3097 (2010).
44. Barnes, R. M. *et al.* Hand2 Loss-of-Function in Hand1 -Expressing Cells Reveals Distinct Roles in Epicardial and Coronary Vessel Development. *Circ. Res.* **108**, 940–949 (2011).
45. Tsuchihashi, T. *et al.* Hand2 function in second heart field progenitors is essential for cardiogenesis. *Dev. Biol.* **351**, 62–69 (2011).
46. Quijada, P., Trembley, M. A. & Small, E. M. The Role of the Epicardium During Heart Development and Repair. *Circ. Res.* **126**, 377–394 (2020).
47. Cao, J. & Poss, K. D. The epicardium as a hub for heart regeneration. *Nat. Rev. Cardiol.* **15**, 631–647 (2018).
48. Cai, C.-L. *et al.* A myocardial lineage derives from Tbx18 epicardial cells. *Nature* **454**, 104–108 (2008).
49. Lajiness, J. D. & Conway, S. J. Origin, development, and differentiation of cardiac fibroblasts. *J. Mol. Cell. Cardiol.* **70**, 2–8 (2014).
50. Doppler, S. A. *et al.* Cardiac fibroblasts: More than mechanical support. *J. Thorac. Dis.* **9**, S36–S51 (2017).

51. Moore-Morris, T., Guimarães-Camboa, N., Yutzey, K. E., Pucéat, M. & Evans, S. M. Cardiac fibroblasts: from development to heart failure. *J. Mol. Med.* **93**, 823–830 (2015).
52. Lees, J., Kong, A., Mitchell, G. & Lim, S. Human Vascularised Cardiac Organoids for Disease Modelling. *Hear. Lung Circ.* **28**, S216 (2019).
53. Tulloch, N. L. *et al.* Growth of engineered human myocardium with mechanical loading and vascular coculture. *Circ. Res.* **109**, 47–59 (2011).
54. Homan, K. A. *et al.* Flow-enhanced vascularization and maturation of kidney organoids in vitro. *Nat. Methods* **16**, 255–262 (2019).
55. Wimmer, R. A. *et al.* Human blood vessel organoids as a model of diabetic vasculopathy. *Nature* **565**, 505–510 (2019).
56. Ma, Z. *et al.* Self-organizing human cardiac microchambers mediated by geometric confinement. *Nat. Commun.* **6**, 1–10 (2015).
57. Kupfer, M. E. *et al.* In Situ Expansion, Differentiation, and Electromechanical Coupling of Human Cardiac Muscle in a 3D Bioprinted, Chambered Organoid. *Circ. Res.* 207–224 (2020) doi:10.1161/CIRCRESAHA.119.316155.
58. Gessert, S. & Kühl, M. The multiple phases and faces of Wnt signaling during cardiac differentiation and development. *Circ. Res.* **107**, 186–199 (2010).
59. Lee, J. *et al.* In vitro generation of functional murine heart organoids via FGF4 and extracellular matrix. *Nat. Commun.* **11**, 4283 (2020).
60. Später, D., Hansson, E. M., Zangi, L. & Chien, K. R. How to make a cardiomyocyte. *Dev.* **141**, 4418–4431 (2014).
61. Kim, M. *et al.* Activin-A and Bmp4 Levels Modulate Cell Type Specification during CHIR-Induced Cardiomyogenesis. 1–16 (2015) doi:10.1371/journal.pone.0118670.
62. Richards, D. J. *et al.* Human cardiac organoids for the modelling of myocardial infarction and drug cardiotoxicity. *Nat. Biomed. Eng.* **4**, 446–462 (2020).
63. Filippo Buono, M. *et al.* Human Cardiac Organoids for Modeling Genetic Cardiomyopathy. *Cells* **9**, 1733 (2020).
64. Gandhi, J. A., Zhang, X. Y. & Maidman, J. E. Fetal cardiac hypertrophy and cardiac function in diabetic pregnancies. *Am. J. Obstet. Gynecol.* **173**, 1132–1136 (1995).
65. Yang, W., Fan, Q. H. & Li, W. A Fully Transparent, Flexible μ ECoG Array Based on Highly Conductive and Anti-reflective PEDOT:PSS-ITO-Ag-ITO Thin Films. in *2020 IEEE 15th International Conference on Nano/Micro Engineered and Molecular System (NEMS)* 124–129 (IEEE, 2020). doi:10.1109/NEMS50311.2020.9265573.

Figures

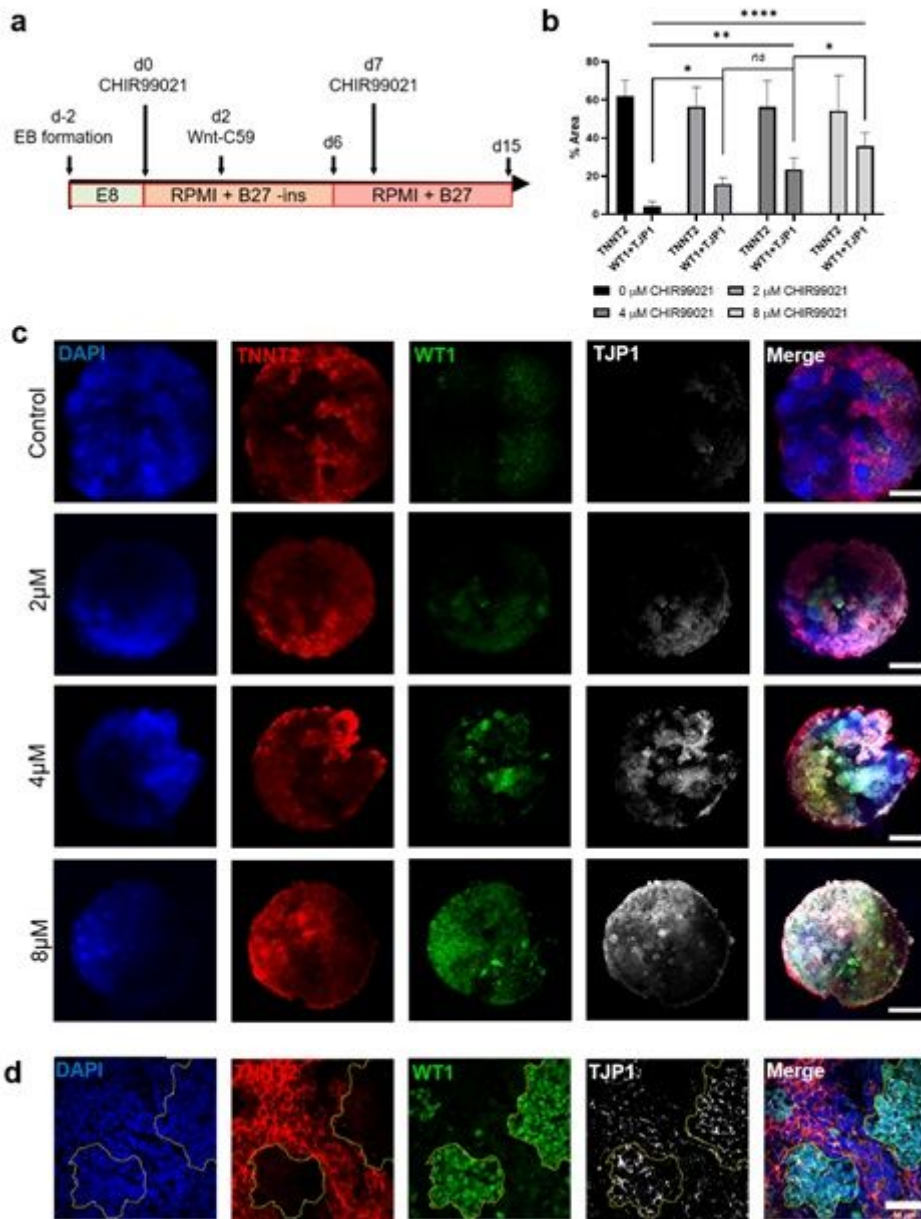


Figure 2

A second CHIR exposure directs epicardial cell differentiation in hHOs. **a**, A schematic diagram depicting the modified protocol used to differentiate TNNT2+ cardiomyocytes and WT1+/TJP1+ epicardial cells in hHOs where x represents the variable CHIR99021 concentration. **b**, Area analysis of cardiomyocyte regions (TNNT2+) and epicardial regions (WT1+ and TJP1+) within organoids taken at multiple z-planes as a percentage of DAPI+ regions of each organoid (n=7 per condition). **c**, Confocal immunofluorescent images of hHOs at differentiation day 15 for DAPI (blue), WT1 (green), TNNT2 (red), and TJP1 (white), with variable concentrations of the second CHIR exposure at day 7 vs control with no second CHIR exposure; scale bars: 500μm, and **d**, high magnification of hHOs with a 2μM second CHIR exposure showing adjacent region of TNNT2+ myocardial tissue and WT1+/TJP1+ epicardial tissue; scale bar: 50μm. (Value = mean ± s.d., two- way ANOVA multiple comparison test; *p<0.05, **p<0.01, ****p<0.0001).

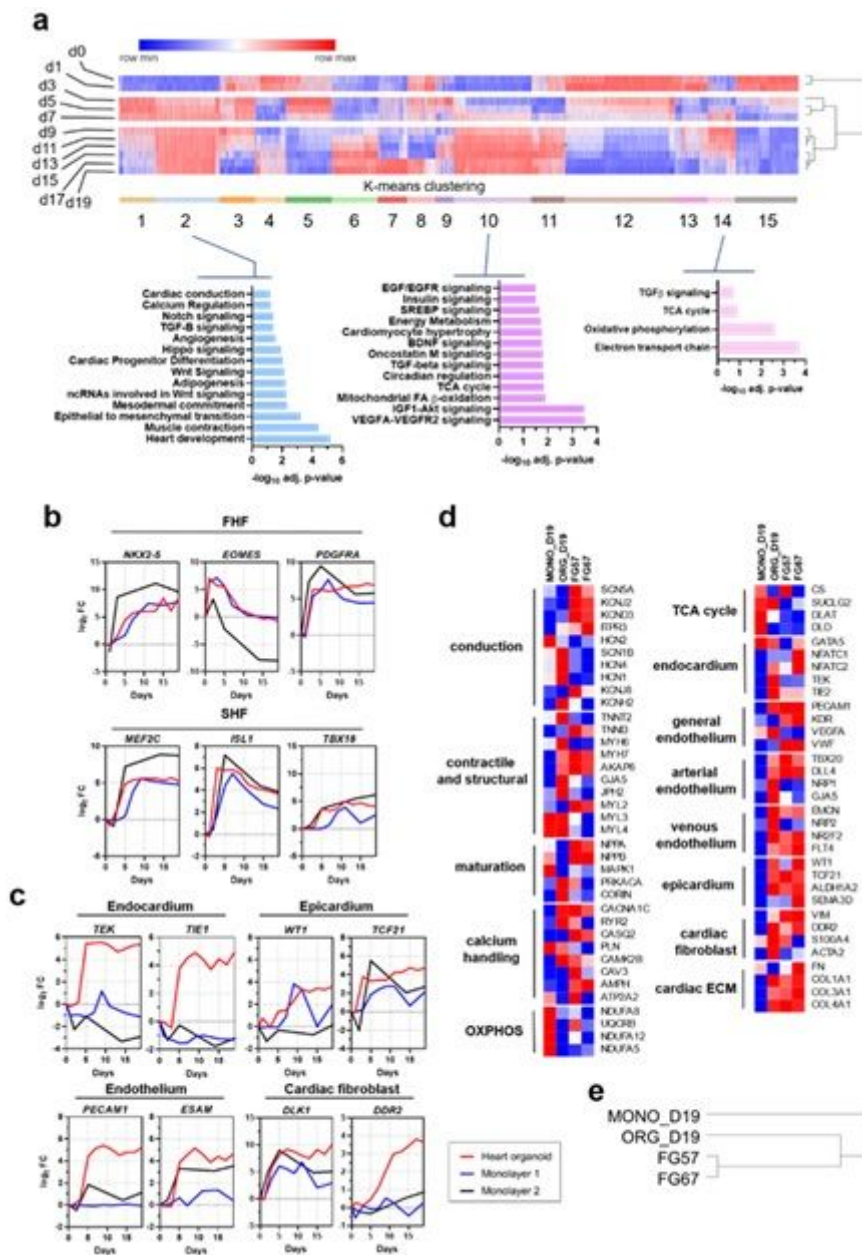


Figure 3

Transcriptomic analysis indicates heart organoids recapitulate multicell type complexity, development and maturation steps similar to embryonic fetal hearts. a, K-means cluster analysis of heart organoid transcriptomes by RNA-seq. Clusters strongly associated with fetal heart development (e.g. 2, 10 and 14) appear from day 9 onwards. Pathway enrichment analysis is provided below for representative cardiac-specific clusters. b, Gene expression analysis (\log_2 fold-change vs. D0) of first and second heart field markers over heart organoid differentiation process (FHF, SHF respectively). c, Gene expression analysis (\log_2 fold-change vs. D0) for cardiac-specific cell type populations in heart organoids, including epicardial cells, fibroblasts, endocardial cells and endothelium. d, Normalized comparison of key genes involved in cardiac function across heart organoids, monolayer differentiation methods, and fetal hearts at gestational day 57-6714. e, Hierarchical clustering analysis of heart organoids, monolayer differentiation and fetal hearts.

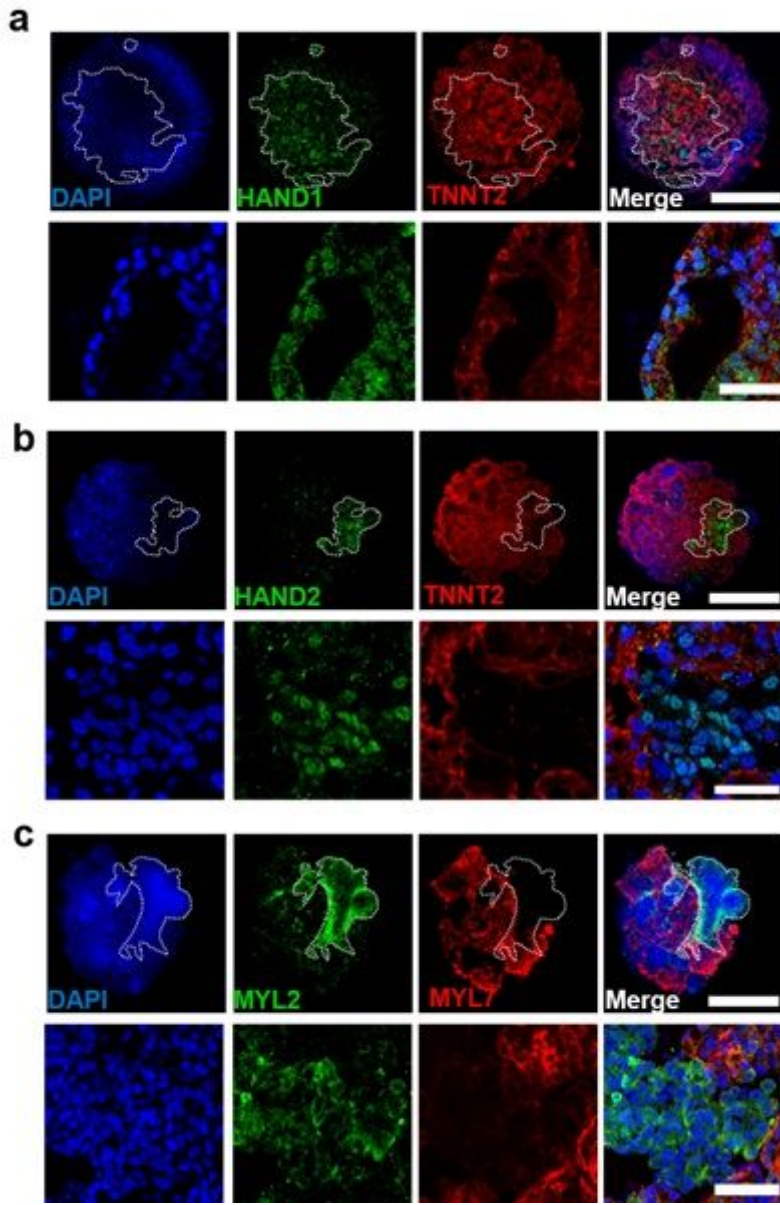


Figure 4

Heart field development and cardiomyocyte specification in hHOs. a-c, Confocal immunofluorescent images of hHOs on Day 8 of differentiation show robust HAND1 (a) and HAND2 (b) transcription factor expression (green), TNNT2 (red), DAPI (blue); Scale bar: 500 μm, inset: 50 μm. c, Confocal immunofluorescent images of day 15 hHOs containing well differentiated ventricular (MYL2, green) and atrial regions (MYL7, red), DAPI (blue); Scale bar: 500μm, inset: 50 μm.

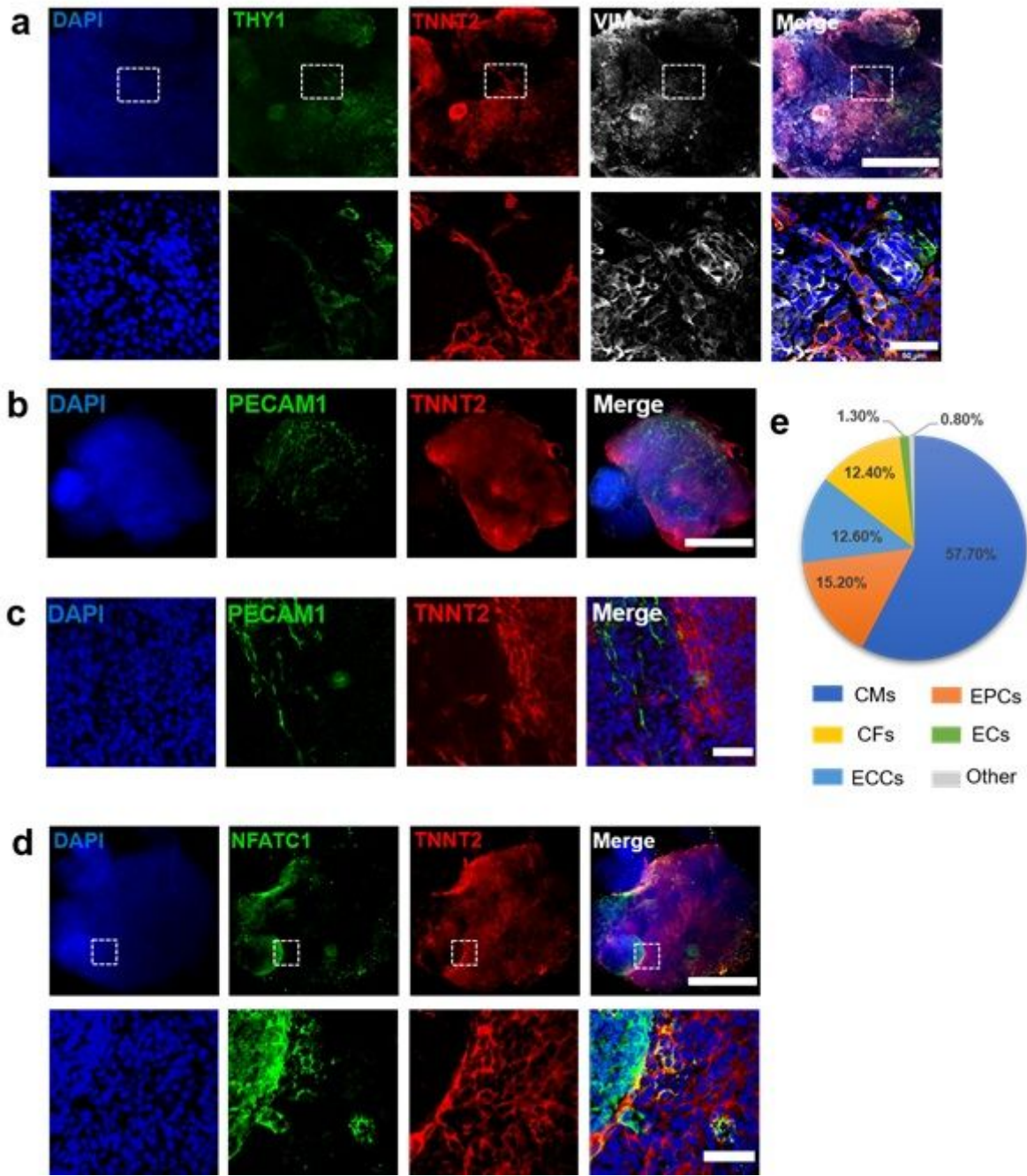


Figure 5

hHO cardiac cell lineage composition. a-d, Immunofluorescence images of various cell lineages composing the hHOs. a, Cardiac fibroblast markers THY1 (green) and VIMENTIN (white) present throughout the hHOs, TNNT2⁺ (red), DAPI (blue); Scale bar: 500 μ m, inset: 50 μ m. b, Endothelial marker PECAM1 (green) showing a defined network of vessels throughout the organoid and adjacent to TNNT2⁺ (red) tissue, DAPI (blue); Scale bar: 500 μ m. c, 60X magnification of PECAM1⁺ endothelial tissue in close proximity to TNNT2⁺ myocardial tissue (scale bar: 50 μ m). d, Endocardial marker NFATC1 (green) highly expressed within microchambers of TNNT2⁺ (red) tissue; scale bar: 500 μ m, inset: 50 μ m. e, Pie chart of average cell composition in hHOs, calculated as the percentage of whole organoid area using ImageJ.

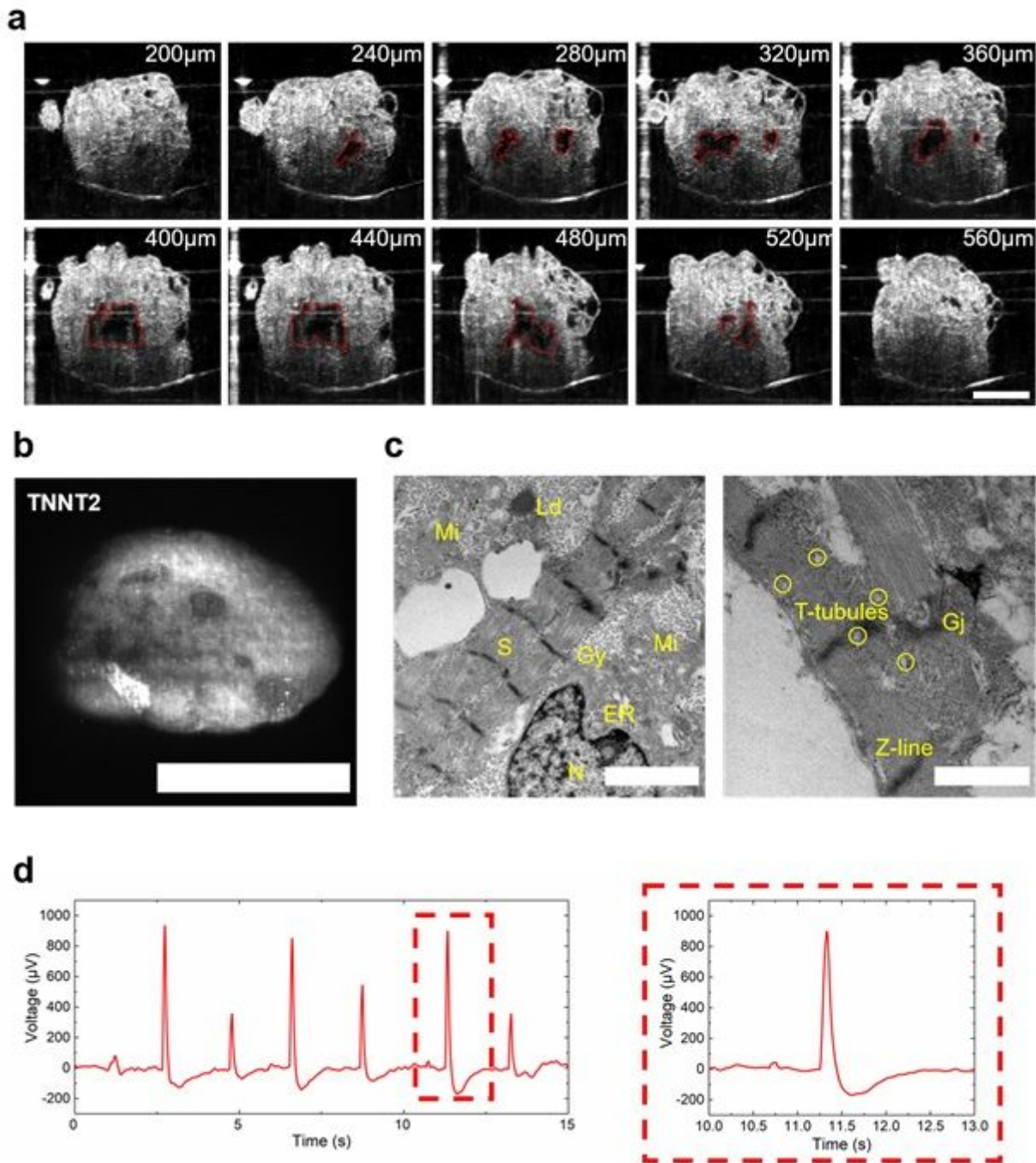


Figure 6

Microchamber formation, ultrastructure and Electrophysiology. a, Optical coherence tomography images showing cross-sections through an organoid, revealing microchambers; scale bar: 500 μm . b, Light-sheet image of hHO stained for TNNT2 with AF488 secondary antibody, revealing chamber structures; Scale bar: 500 μm . c, TEM images of hHOs showing endoplasmic reticulum (ER), gap junctions (Gj), glycogen granules (Gy), lipid droplets (Ld), mitochondria (Mi), nucleus (N), and sarcomeres (S); scale bars: 2 μm (left) 1 μm (right). d, Electrophysiology recordings of organoid on microelectrode array showing 15 seconds (left) and a representative action potential wave (right).

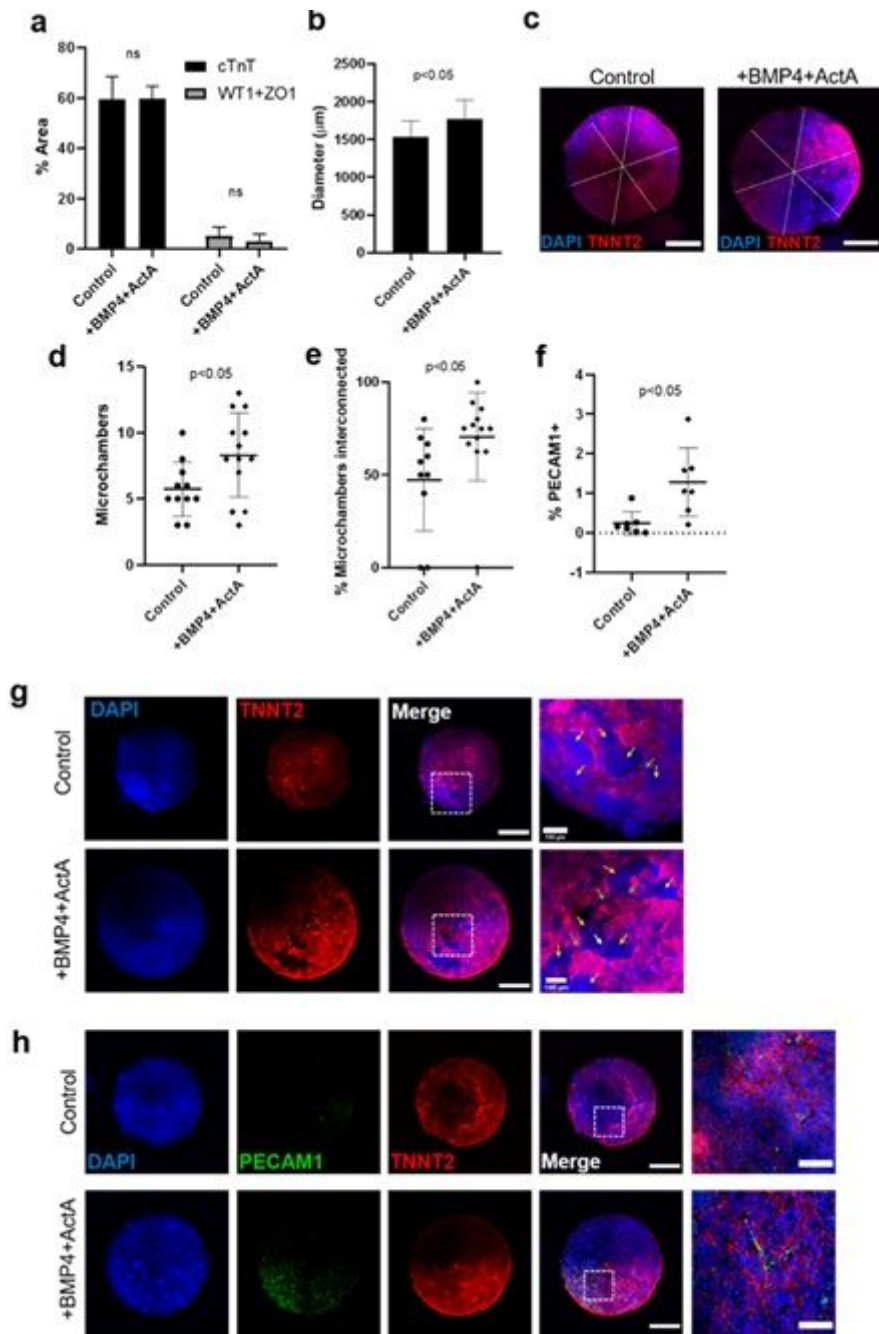


Figure 7

BMP4 and Activin A affect cardiac differentiation and development. a-h, All panels compare hHOs differentiated with CHIR alone (Control) and with CHIR+BMP4+Activin A (Treated). a, Area of cardiomyocyte and epicardial positive regions as a percentage of total organoid area and b, organoid diameter, ($n=8$ per condition). c, Dashed lines showing the diameter of a control (left) and treated (right) organoid averaged to determine the diameter. d-e, $n=12$ per condition. d, Number of microchambers in TNNT2+ areas, and e, interconnectivity of microchambers measured by separation of microchambers by thin TNNT2+ filaments or by thin channels showing clear connection. f, PECAM1+ tissue as a percentage of total organoid area, (measured using MaxEntropy threshold on ImageJ and analyzed all particles of $25\mu\text{m}^2$ to avoid small speckles, $n=7$ per condition). g, Immunofluorescence images of hHOs showing interconnected microchambers (yellow arrows), TNNT2+ filaments (white arrows), and channels

connecting microchambers (green arrows), DAPI (blue), TNNT2 (red), scale bar: 500 μ m, inset: 100 μ m h, Immunofluorescence images of hHOs showing DAPI (blue), PECAM1+ tissue (green), and TNNT2+ tissue, scale bar: 500 μ m, inset: 50 μ m. (Value = mean \pm s.d., two-tailed, unpaired t-test).

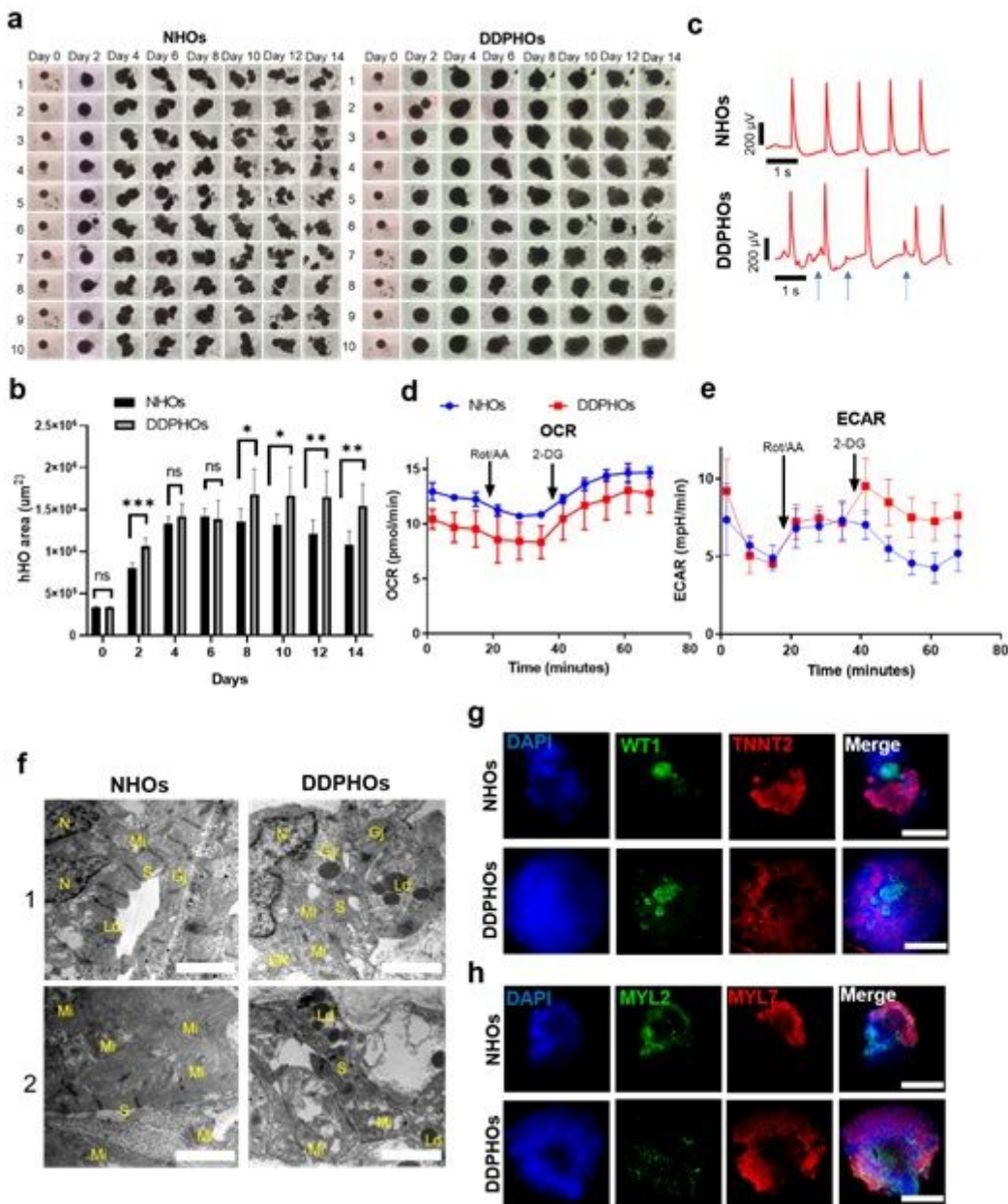


Figure 8

Human heart organoids faithfully recapitulate hallmarks of DDP-induced CHD. a, Brightfield images following development of 10 hHOs under normal glycaemic conditions (NHOs, left) and under diabetic conditions (DDPHOs, right) over two weeks of differentiation. b, Area of hHOs in the first two weeks of differentiation (mean \pm SD; n=12; 2-way ANOVA Sidak's multiple comparisons test). c, Electrophysiology was performed on NHOs and DDPHOs at 15 days. Arrows indicate arrhythmic events. d, Seahorse analysis for oxygen consumption rate (OCR), and e, extracellular acidification rate (ECAR) of normal and diabetic hHOs. f, Ultrastructural analysis by TEM of NHOs and DDPHOs showing endoplasmic reticulum (ER), gap junctions (Gj), glycogen granules (Gy), lipid droplets (Ld), mitochondria (Mi), nucleus (N), and

sarcomeres (S). g, Confocal immunofluorescent images at differentiation day 15 for cardiac (TNNT2) and epicardial (WT1) formation. h, Confocal imaging for ventricular (MYL2) and atrial (MYL7) chamber formation under normal and diabetic-like conditions. Scale bar: 500 μ m.

Supplementary Files

This is a list of supplementary files associated with this preprint. Click to download.

- [Supplementaryinformationfinal.pdf](#)
- [supplvideo1.avi](#)
- [supplvideo2.avi](#)
- [supplvideo3.avi.avi](#)
- [supplvideo4.avi.mp4](#)
- [supplvideo5.avi.mp4](#)
- [supplvideo6.avi.mp4](#)
- [supplvideo7.avi.mp4](#)
- [supplvideo8.avi.mp4](#)
- [Suppl.DataTable1.xlsx](#)
- [AitorAguirreSupplementaryinformationfinal.docx](#)